Electronic Supplementary Material (ESI) for Physical Chemistry Chemical Physics.

Supplementary Information

Kinetic Monte Carlo simulations of organic ferroelectrics

Tim D. Cornelissen, Michal Biler, Indre Urbanaviciute, Patrick Norman, Mathieu Linares, Martijn Kemerink

Contents

Model details

Energy calculations

As stated in the main text, we consider a collection of dipoles whose position is fixed by the morphology of the material, as shown in Fig. S1. To determine the flipping probability of a dipole, we calculate the energy difference between the initial and final state using electrostatics. The electric field caused by neighboring dipole $\vec{\mu}_j$ at the position of $\vec{\mu}_i$ is given by:

$$\vec{E}_{ij} = \frac{1}{4\pi\epsilon_r\epsilon_0 r_{ij}^3}\left[\vec{\mu}_j - 3\hat{r}_{ij}\left(\vec{\mu}_j \cdot \hat{r}_{ij}\right)\right], \quad \text{Eq. S1}$$

with $\epsilon_r\epsilon_0$ the permittivity of the material and $\vec{r}_{ij} = r_{ij}\hat{r}_{ij}$ the vector separating the two dipoles. These interactions are calculated up to a certain cut-off distance r_c. The long-range interactions outside r_c are approximated using the reaction field method [1]. This method assumes that the molecules within r_c induce a polarization in the surrounding material with dielectric constant ϵ_r. This polarization creates a reaction field at the position of the dipole:

$$\vec{E_{RF}} = \frac{2(\epsilon_r - 1)\vec{M}}{2\epsilon_r + 1\, r_c^3}, \quad \text{Eq. S2}$$

with $\vec{M} = \sum_i \vec{\mu}_i$ the sum over all dipoles within r_c. Including the applied field, the energy of dipole *i* then reads

$$U_i = -\,\vec{\mu}_i \cdot \left(\vec{E_{RF}} + \vec{E_{applied}} + \sum_{\substack{j \\ r_{ij} < r_c}} \vec{E}_{ij}\right). \quad \text{Eq. S3}$$

On top of the permanent dipoles μ_0 of the amide groups, we should also consider induced dipoles μ_{ind}. Unlike the permanent dipoles, these induced dipoles are not restricted to only two fixed orientations, as they will lie along the direction of the local field $\vec{E_{loc}}$:

$$\vec{\mu_{tot}} = \vec{\mu}_0 + \vec{\mu_{ind}} = \vec{\mu}_0 + \alpha * \vec{E_{loc}}, \quad \text{Eq. S4}$$

with α the electronic polarizability. This local field is dependent on the surrounding dipoles, which in turn are dependent on their local fields. This leads to a self-consistent problem that is solved iteratively (see Fig. S2 for the convergence).

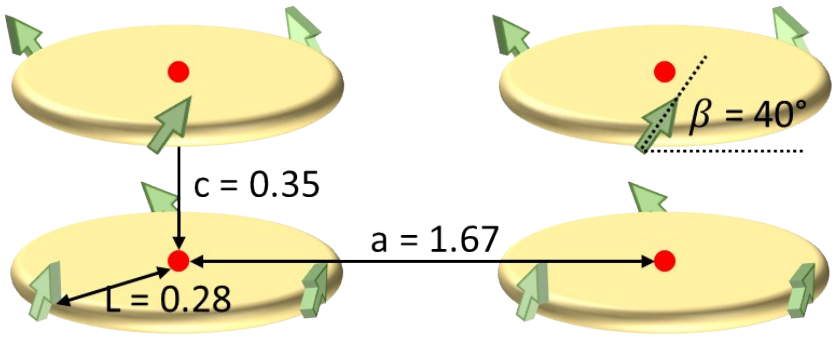

Fig. S1. The geometry of BTA with typical distances given in nm.

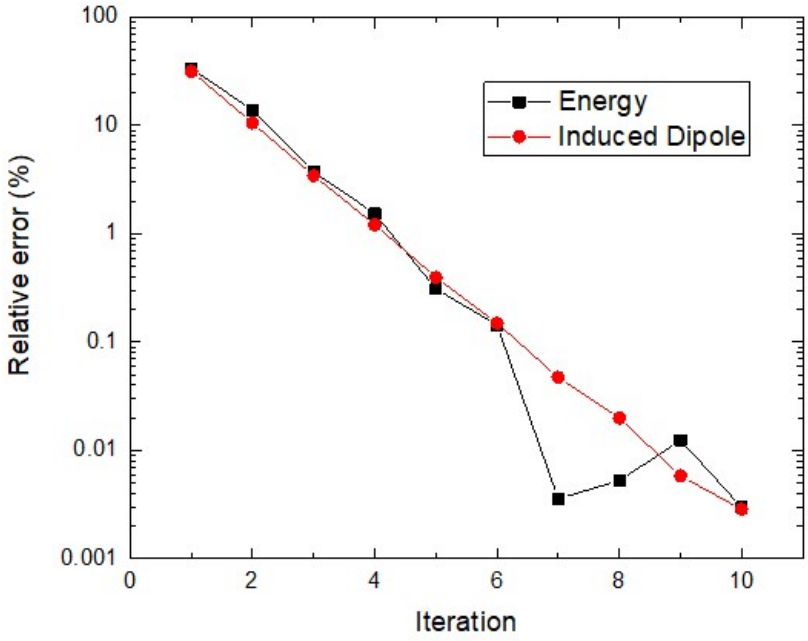

Fig. S2. Convergence of the induced dipole calculation. Both the energy of the whole system and the induced dipole show an exponential convergence.

Monte Carlo algorithm

The dynamical behavior of the system is simulated using a kinetic Monte Carlo method. The flipping probability ν of a dipole is calculated by assuming thermal activation over an energy barrier:

$$\nu = \begin{cases} \nu_0 \exp\left(-\frac{\Delta U}{k_B T}\right), & \Delta U > 0 \\ \nu_0, & \Delta U \leq 0 \end{cases}, \qquad \text{Eq. S5}$$

with ν_0 the attempt frequency, which is taken to be a typical phonon frequency of the system, $k_B T$ the thermal energy, and ΔU the energy difference between the initial and final state as calculated using the equations above.

The numerical algorithm is now as follows:

1. Initialize the position and orientation of all dipoles, iteratively calculate the induced dipoles, and determine all flipping rates.
2. Use a weighted random choice based on the flipping rates to pick a dipole to flip.
3. Flip the chosen dipole and add $\Delta t = \ln(x)/\nu_{total}$ to the simulation time, with x a random number between 0 and 1, and ν_{total} the sum of all individual flipping rates.
4. Update all induced dipoles and flipping rates.
5. Go back to step 2 until a stop condition is met.

This algorithm allows us to simulate the non-equilibrium dynamics of the dipoles with the correct time scales, both with and without applied field.

The total polarization of the system is calculated by summing the *z*-component of all permanent and induced dipoles.

Boundary conditions

From the morphology as shown in Fig. 1 of the main text we find the position and orientation of the dipoles, which remain fixed during the simulations. We consider a capacitor structure as it is used in experiments, with the active material sandwiched between two parallel electrodes. Two different types of boundary conditions are therefore used. In the *xy*-plane parallel to the electrodes we take periodic boundaries, representing an infinitely large thin film. In the *z*-direction, perpendicular to the electrodes, we use the method of mirror images. The electrodes are assumed to provide perfect screening, so that each dipole is reflected in the 'mirror' of the electrode.

Parameters

In table S1 the set of default simulation parameters is given. Fig. S3 gives a schematic overview of the disorder parameters. The distance between the columns is a on average, but a random offset drawn from a parabolic distribution with width σ_{xyz} is added. Each column is divided into subcolumns with length $N \pm \sigma_N$. Between two subcolumns there is a defect that consists of a translational offset in all three coordinates. The size of the offset is randomly drawn from a distribution with again width σ_{xyz}. Each subcolumn also has its own rotational angle and helicity.

Table S1. Default simulation parameters, corresponding to 'medium' disorder.

	Parameter	Value	Unit
Morphology	Helical pitch	6	molecules
	OOP rotation β	40	degrees
	Hexagonal packing distance a	1.67	nm
	Interdisc distance c	0.35	nm
	Dipole distance from center *L*	0.28	nm
Disorder	Subcolumn length N	15	molecules
	Subcolumn length disorder σ_N (Parabolic width)	2	molecules
	Positional disorder σ_{xyz} (Parabolic width)	0.01	nm
Simulation	Box size in the x direction	8	molecules
	Box size in the y direction	8	molecules
	Box size in the z direction (column length)	30	molecules
	Interaction cut-off range	40	dipoles

	Total amount of dipoles	5760	dipoles
Material	Permanent dipole moment μ	4	D
	Polarizability α	1	eÅ²/V
	Temperature T	350	K
	Phonon frequency ν_0	1	THz
	Effective permittivity ϵ_r	2	-

The permittivity of a dipolar material like BTA has two main contributions: a dipolar and an electronic part. The dipolar part is substantial and is the cause of the high permittivity found in ferroelectrics. However, we can ignore this part, because we explicitly calculate the interactions between the dipoles. The electronic contribution to the permittivity is smaller, but this is the effective permittivity we need to use for our electrostatic calculations. Based on previous DRS measurements[2] and simulation work we estimate a value of $\epsilon_r =$ 2.

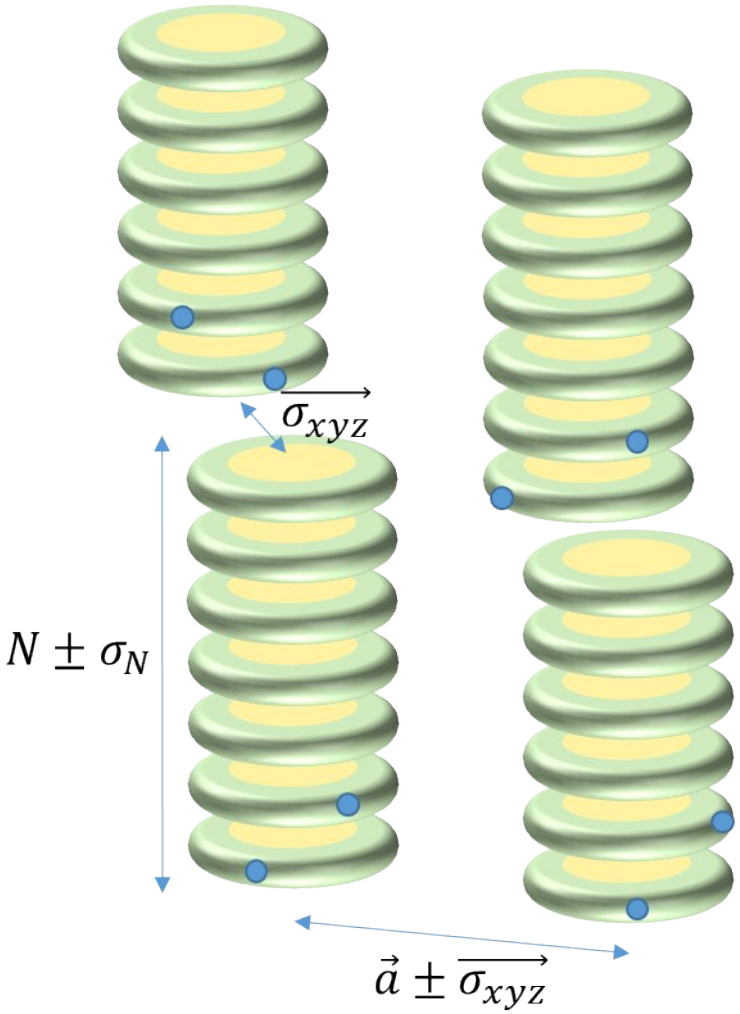

Fig. S3. Schematic representation of the way disorder is introduced in the system. The dots indicate the helicity and rotational angle of a subcolumn.

Permanent and induced hysteresis loop

As stated in the main text, the polarization has two components, that of the permanent and induced dipoles. As shown in Fig. S4, both components show hysteretic behavior. In the loop of the induced dipole there is also a linear background that corresponds to the dipole moment induced by the applied field. In experiments this background is corrected with the Double-Wave Method (DWM), which uses two field pulses in succession: one to measure the switching polarization plus the non-switching background, and one to measure only the non-switching background. To enable comparison with the experiments, we also subtract the background from the simulated loops.

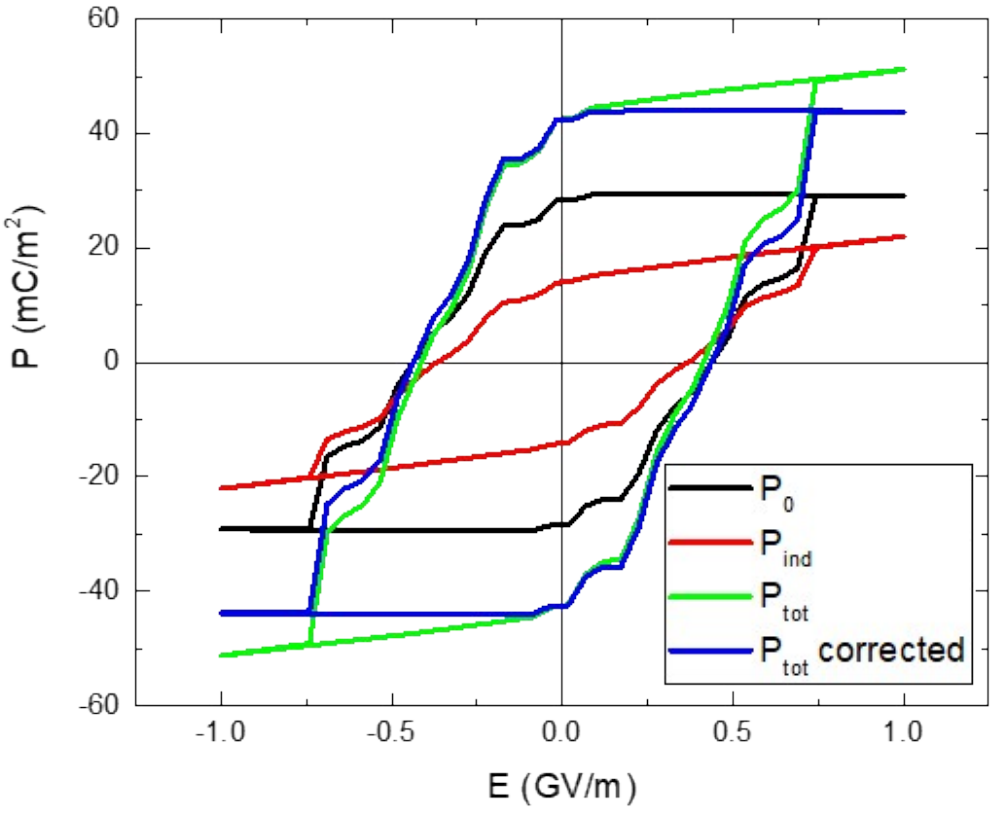

Fig. S4. The different contributions to the polarization hysteresis loop. The permanent (black) and induced (red) dipoles add up to the total polarization (green). Subtraction of the linear background gives the final loop (blue).

Depolarization curves

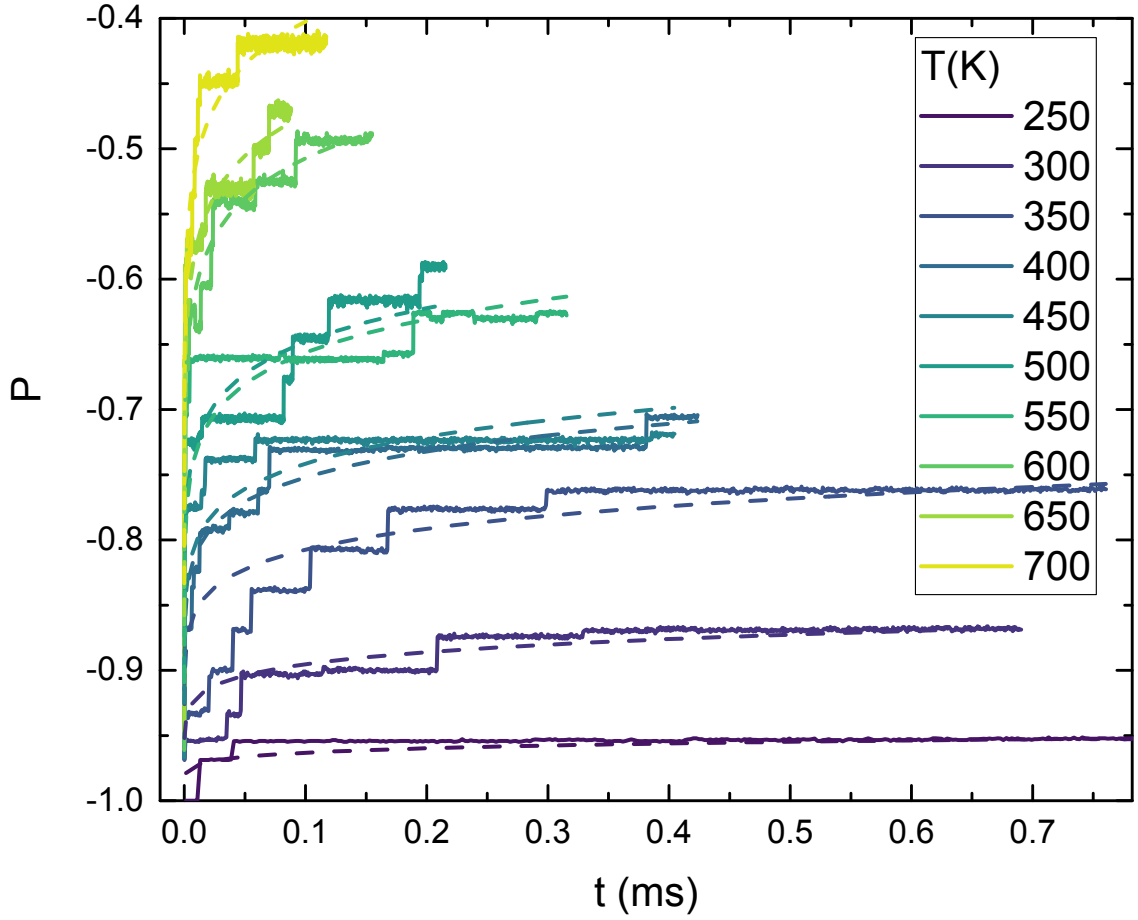

Fig. S5. Depolarization curves for different temperatures, fitted to Eq.(2).

Full flip mode and the 2:1 state

For the full flip mode, we have also calculated the coercive field as a function of both temperature and frequency. Fig. S6 shows the equivalent of Fig. 3 in the main text, now with the simulation restricted to the full flip mode.

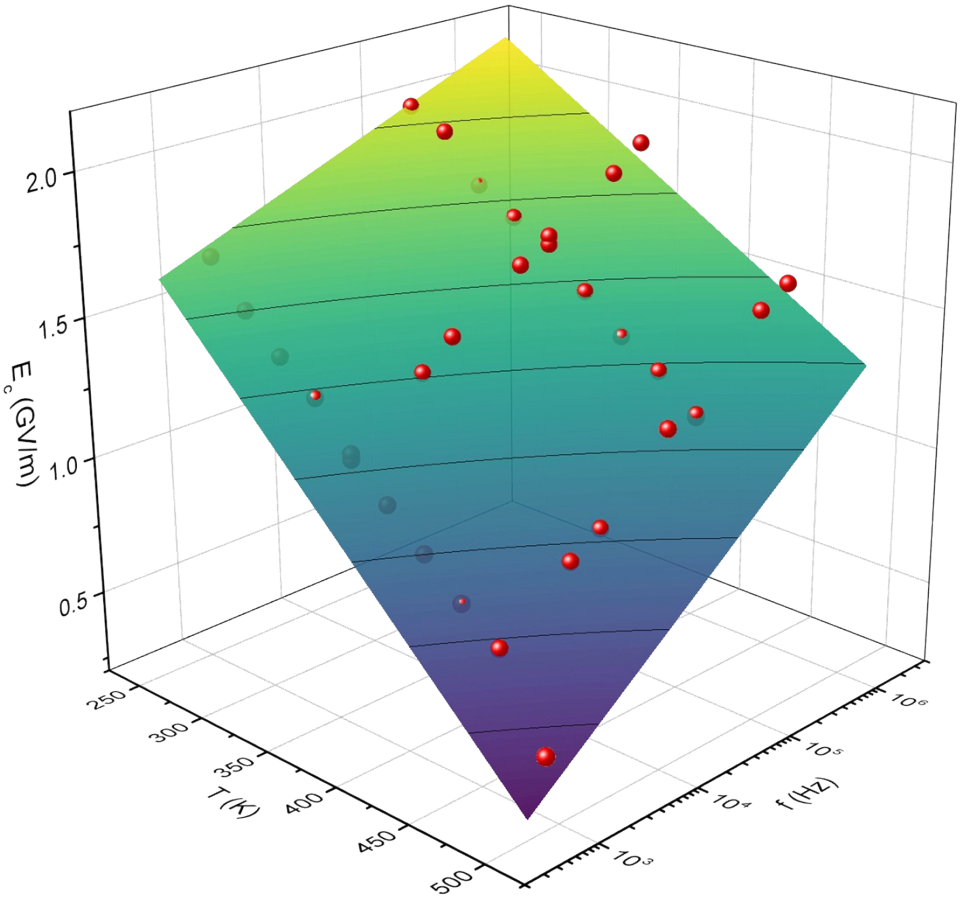

Fig. S6. The coercive field as a function of frequency and temperature from simulations with the full flip mode (symbols). The surface is a fit to the data of Eq. (1) with $w_b = 0.89$ eV/nm³, $V^* = 1.12$ nm³, and fixed $P_s = 48$ mC/m² and $\nu_0 = 1$ THz.

In the main text (Fig. 5) it was shown that there exists a shoulder in the hysteresis loop of the full flip mode, corresponding to a 2:1 state of the dipole helices. A snapshot of this state is shown in Fig. S7. The shoulder can be explained by considering the energy landscape in Fig. S8. We know from literature that the 1:2 and 2:1 states are energetically favorable over the 3:0 and 0:3 if there is no externally applied field[3–5], which results in the energy landscape in Fig. S8(a). It has four potential wells, an energy difference of dF between the 3:0 and 2:1 state, and an energy barrier W_b which is assumed to be equivalent between all states. Starting in the 3:0 state, this energy barrier prevents the transition to the 2:1 state provided the thermal energy is small. When an electric field is applied, the barrier will at some point become small enough to be overcome by thermal fluctuations and the system will go to the 2:1 state (Fig S8(b)). Now also the next barrier can be overcome, and the system will immediately transition into the 1:2 state, which is the global

energy minimum at that point. The system remains in this state, which corresponds to the shoulder in the hysteresis loop, until the field is increased sufficiently to make the 0:3 state the most favorable (Fig S8(c)).

It is worth to note that the shoulder becomes more pronounced when disorder is absent, see Fig S9. This can be explained with the same argument as was used in the main text to explain the increased slanting of the loops with increasing disorder. Due to the disorder, there are no longer two well-defined fields at which the whole system will switch from 2:1 to 1:2 to 3:0, but there will be a distribution in these coercive fields. These distributions will slightly overlap, leading to a less pronounced shoulder in the disordered case of Fig. 5(b).

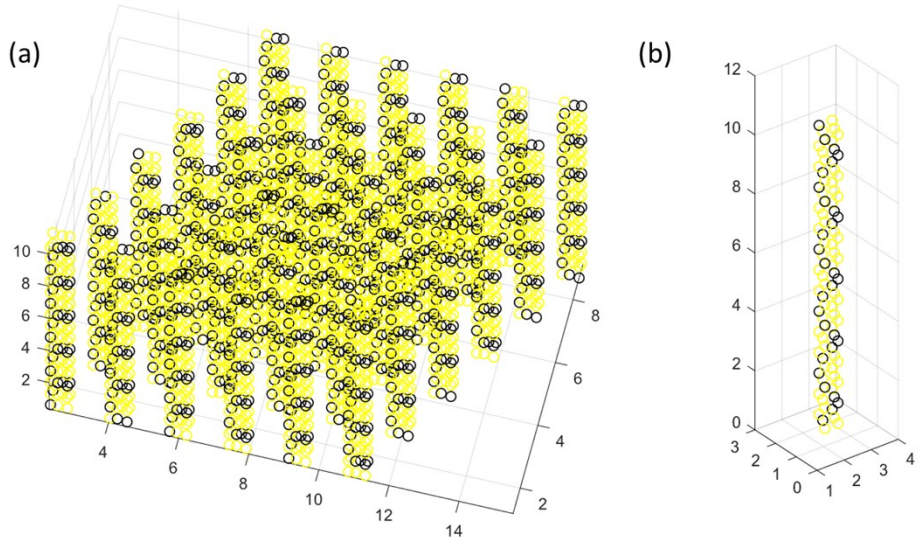

Fig. S7. A snapshot of the simulation while it is in the 1:2 state, showing (a) the whole box and (b) a single column. Each dot represents a dipole, and its color indicates whether it is pointing up (black) or down (yellow).

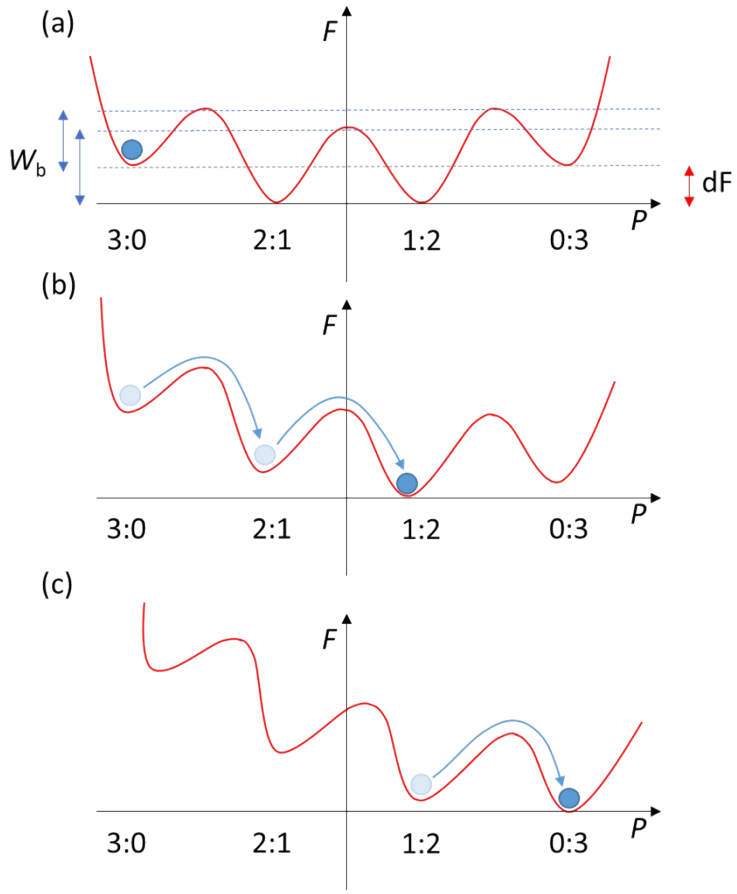

Fig. S8. Free energy landscape with the four possible polarization states. From (a-c) the applied field is increased to favor the 0:3 positive polarization state. (a) The initial 3:0 state with negative polarization. The energy barrier between states is W_b and the energy difference between the 3:0 and 2:1 states is dF. (b) When the applied field is slightly increased, the system will go through the 2:1 state and end up in the 1:2 state. (c) When the field is further increased, the 0:3 state is reached.

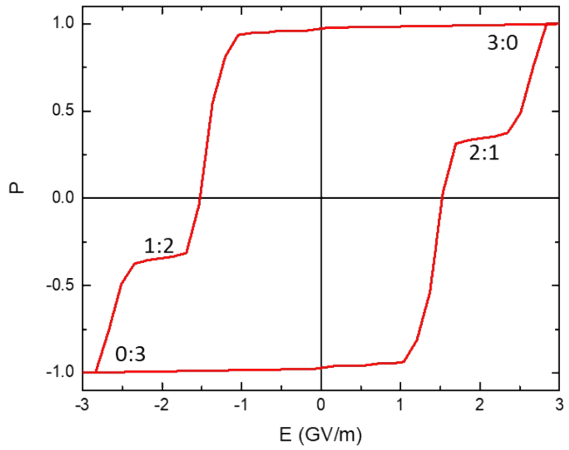

Fig. S9. Hysteresis loop for the full flip mode in a system without disorder.

Molecular dynamics simulations

Computational Details

All molecules were optimized within the density functional theory formalism using the Gaussian software package;[6] the Ante_R.E.D. program[7-9] with B3LYP/cc-pVDZ was used to calculate ESP charges; topology and initial coordinate files were generated by the LEaP program with a general amber force field (GAFF).[10] The system was first minimized to find the appropriate box size in the z-direction, after which it ran for 10 ns in an NVT ensemble at 300 K using Langevin dynamics. Subsequently, we applied a series of electric fields with different strengths (0.001, 0.01, 0.035, 0.065, 0.11, 0.22, 0.28, 0.36, 0.43, and 1.0 V/nm) in both (+) and (-) directions with respect to the z-axes, and we let the MD simulations run again in NVT ensemble at 300 K for about 70 ns with a time step of 2 fs per step. The trajectories were recorded every 5000 steps and the cut-off was set to 12 Å for non-bonded interactions. All MD simulations were carried out using either Amber 14 or Amber 16 force field.[11,12]

We constructed two BTA self-assemblies: one made of 22 BTA molecules in order to have a 3:0 rotamer (with minimized distance between BTA molecules being 3.316 Å), and the second made of 24 BTA molecules to have a 2:1 rotamer (3.356 Å per one BTA). The 22 and 24 BTAs were chosen to be able to apply periodic boundary conditions, and since the BTAs are twisted about 60° with respect to each other to keep the hydrogen bond network, the number must be a multiple of two and six for 3:0 and 2:1, respectively. Although our simulations started from P-helical BTA H-network conformation (clockwise, where BTA helicity is right-handed to form hydrogen bonds with the residues under and above, Fig. 5 in the main text), assemblies may adopt both P- or M-helicity (anti-clockwise with left-handed helicity).

In order to evaluate MD simulations, we chose three dihedral angles (ϕ1, ϕ2, ϕ3) to follow the conformations 3:0 *vs.* 2:1, and P *vs.* M. At the very beginning of the MD simulations, all C=O and N-H moieties pointed below and above the plane, respectively, with dihedral angles being around 30° for 3:0 rotamer in P- conformation. For the 2:1 rotamer in P-conformation, one C=O was oriented in the opposite direction (above the plane) with respect to the other two moieties, therefore the corresponding dihedral angles were around -150°, 30° and 30°.

3:0 state

External electric field (EE) applied in the (+)-direction had no effect on the assembly as the system still remained in the 3:0 orientation, whereas the (-)-direction of EE switched the orientation from 3:0 to 0:3 rotamer. Indeed, after applying EE = 0.22 V/nm, dihedral angles switched from around 30° to -30° (Fig. S10a). All C=O moieties switched at the similar moment. Moreover, the helicity was changed from P to M. Lower electric fields (below 0.11 V/nm) had no significant effect on the dihedral angles.

2:1 state with electric field in (+)-direction

No specific effects were observed with EE below 0.28 V/nm. Only electric field of 0.36 V/nm induced a change from the 2:1 to 3:0 rotamer keeping the same helicity. Considering the values of dihedral angles, ϕ1 and ϕ2 remained unaffected, hence their values were still around 35°. The ϕ3 turned from around -145° to 35°; in other words the C=O moiety turned about 180° and a higher EE was required to induce this change compared to the 3:0 rotamer, for which the dihedral angles turned only by about 60° and slightly lower EE was sufficient to induce the switch.

2:1 state with electric field in (-)-direction

Although no specific macroscopic effects were seen for EE below 0.28 V/nm as we still kept the 2:1 P-conformer, small microscopic changes were observed. First, one of the three dihedral angles of one of the residues in the stack changed from around -145° to 35°, then the second one remained around 35°, and finally the third one went from 35° to -145° (Fig. S10b). This went with a twist of the residue to keep the network of hydrogen bonds with the adjacent molecules. Intermediate states exist at E = 0.36 V/nm; in other words both 0:3 P-helical BTA (dihedral angles being around -145°) and M-helical BTA (dihedral angles being around -35°) were observed. One half of the 24-stacked self-assembly remained in the anti-clockwise orientation, whereas the other half switched to the clockwise orientation. Since the electric field is not high enough to keep a favorable orientation and helicity, some of the residues may have gotten from P- to M- and back from M- to P-helical BTA (Fig. S10d). Other residues switched to 1:2 rotamer orientation with or even without favorable H-bonding systems. These intermediate states occurred only for a short time. When the external electric field increases to 0.43 V/nm, no intermediate states exist anymore and the self-assembly is fully switched from 2:1 to 0:3 with anti-clockwise helicity. Here, all three C=O moieties underwent a change of their dihedral angles (from -145° to -30°, 30° to -30° and 30° to -30°), which required slightly higher field then the previous case of 2:1 rotamer with electric field in (+)-direction.

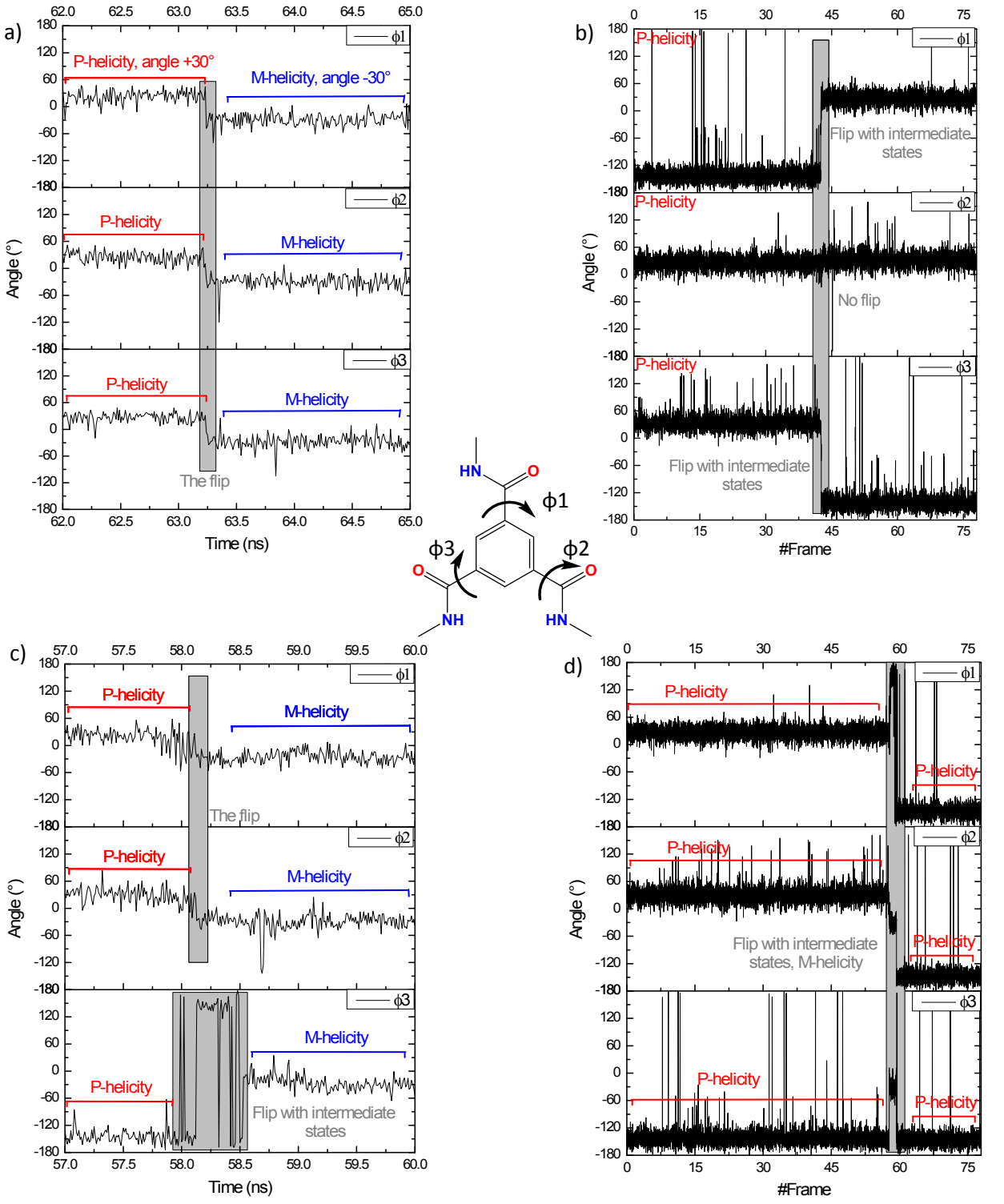

Fig. S10. Time evaluation of the most representative dihedral angles of three C=O groups for a) the 3:0 rotamer at EE = 0.22 V/nm, and the 2:1 rotamer at b) EE = 0.22 V/nm, c-d) EE = 0.36 V/nm. Evolution of ***c***, and ***d*** corresponds to different residues within the stack. In the middle: Studied structure with highlighted dihedral angles.

The effect of disorder

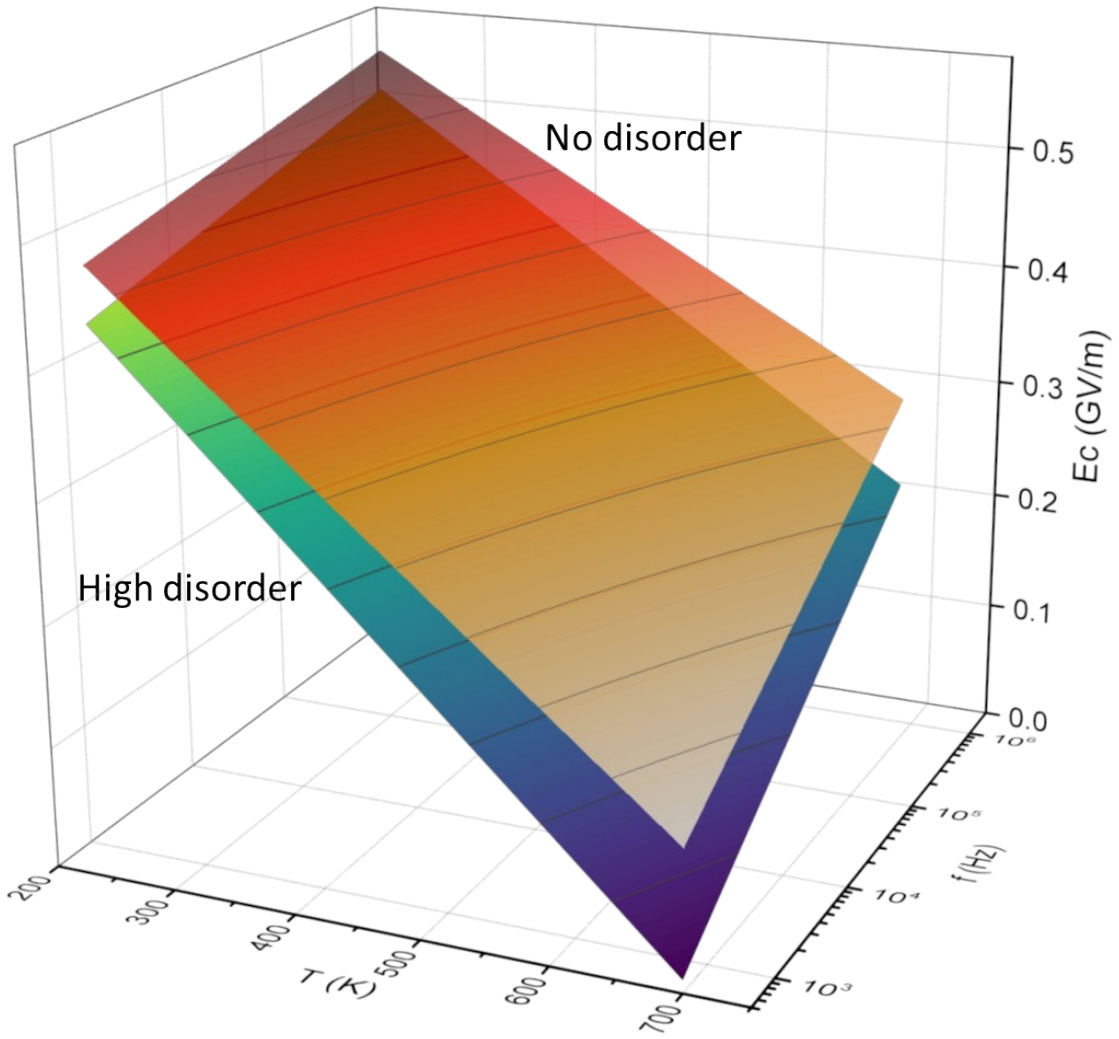

Fig. S11. The coercive field as a function of temperature and frequency for two different cases of disorder. The high disorder case (rainbow) has a subcolumn length of $N = 7$, the no disorder case (brown) has no subcolumns. Only a slight difference in coercive field is observed over the whole parameter range.

Nucleation

In the main text the different effects of disorder on the retention and the coercive field is attributed to a difference in nucleation mechanism. During a hysteresis loop, nucleation occurs at the electrodes, while during depolarization it occurs at defects. This can be explained by looking at the energy landscape in Fig. S12. It shows for each dipole, within a specific column with a defect, how much energy it would cost to flip it. The black baseline, which corresponds to all dipoles pointing in one direction, shows that a single dipole flip preferentially happens at the electrodes. A flip could also occur at the defect, but at a much lower rate since the flipping rate exponentially depends on the energy (see Eq. S5).

During depolarization, so without applied field, if a dipole flips near the electrode (#1, vertical dashed red line) the red line in Fig. S12(a) is obtained. There is thus a very high chance that that dipole flips back to its original orientation in the next step of the simulation. The single flipped dipole at an electrode is thus unstable. In contrast, when a dipole flips near the defect (#43, vertical dashed blue line), there is a significant chance that in the next step a neighboring dipole will flip as well as seen from the peak in the dashed blue curve for dipole #48. From these two dipoles, the nucleus can grow further. So even though flipping at the defect is less frequent than at the electrodes, only flipping at a defect will result in a stable nucleus, and polarization reversal will thus occur through nucleation at the defect.

This picture changes when an electric field is applied, such as during the measurement of a hysteresis loop. Now the red line in Fig. S12(b) shows that after the initial flip at the electrode, there are two neighboring dipoles (#4 and #6) that will most likely flip in the next steps. A stable nucleus can now be formed at an electrode. Flipping near the defect still results in a stable nucleus as well but since a flip near an electrode is more likely to begin with, polarization reversal will now occur through nucleation at the electrodes.

After this first nucleation step, the nucleus needs to grow further until it reaches the critical size threshold, after which the rest of the column flips near instantaneously. This critical nucleus is slightly smaller when a field is applied, which we speculate to be the cause of the different observed attempt frequencies, as discussed in the main text and Fig. 6.

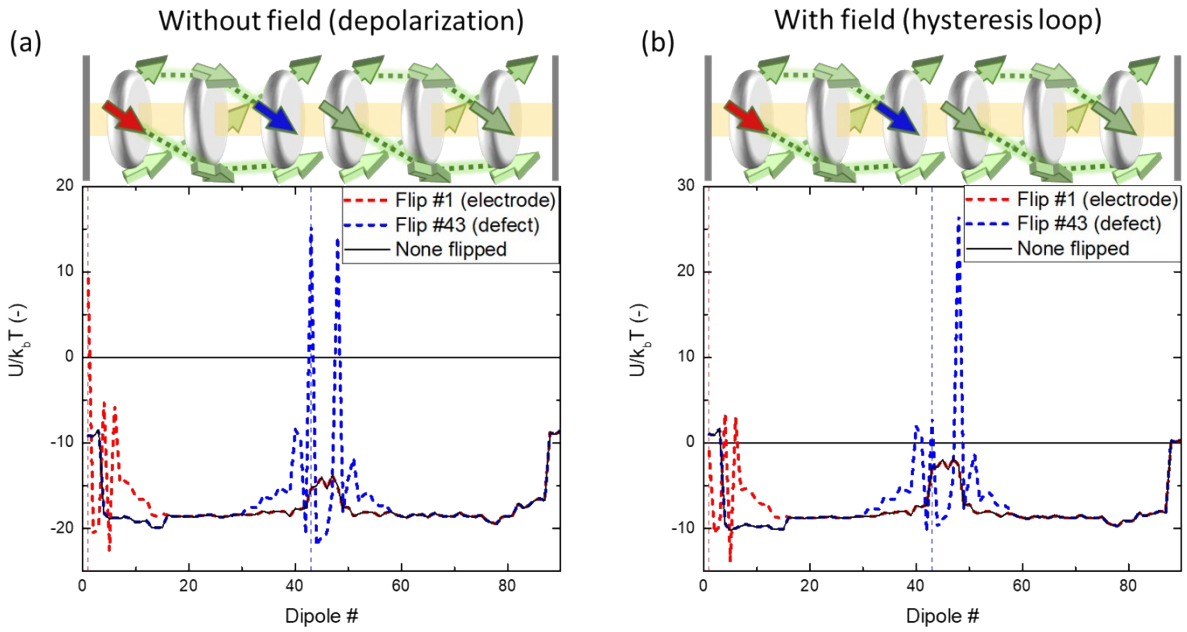

Fig. S12. Energy needed for flipping a single dipole as a function of position in a column for the situation (a) without and (b) with applied field of 1 GV/m. A more positive energy means that a dipole is energetically more favored to flip. The column is schematically shown above the graphs (not to scale), with electrodes at both ends and a defect in the middle. The black curve is for all dipoles in one direction, the red and blue dashed curve correspond to the energies after flipping a dipole at the electrode (#1, vertical dashed red line) and the defect (#43, vertical dashed blue line) respectively.

Ground state

There are several ways to obtain the ground state of the system. The first is to let a simulation of the depolarization process run until equilibrium is reached (with $P = 0$). Due to computational constraints, this is only possible for highly elevated temperatures where the depolarization process is fast. We therefore first let the system depolarize at 2000 K and subsequently let it stabilize at 350 K. However, this might not result in the true ground state as 2000 K might be above the Curie temperature of the system. We therefore also run a simulation starting from a $P = 0$ state with all dipoles randomly oriented, and let it run at 350 K until again an equilibrium is reached. Both methods gave nearly identical results, suggesting that it truly is the ground state that is obtained.

We can use correlation coefficients to characterize the interactions in the ground state in Fig. 7. The correlation coefficient of a dipole *i* is given by:

$$C_i = \sigma_i \sum_{j \epsilon NN} \sigma_j \qquad \text{Eq. S6}$$

where the sum goes over all (next) nearest neighbors. When the correlation coefficient is negative, neighboring dipoles tend to be antiparallel, as shown in Fig. S12(a).

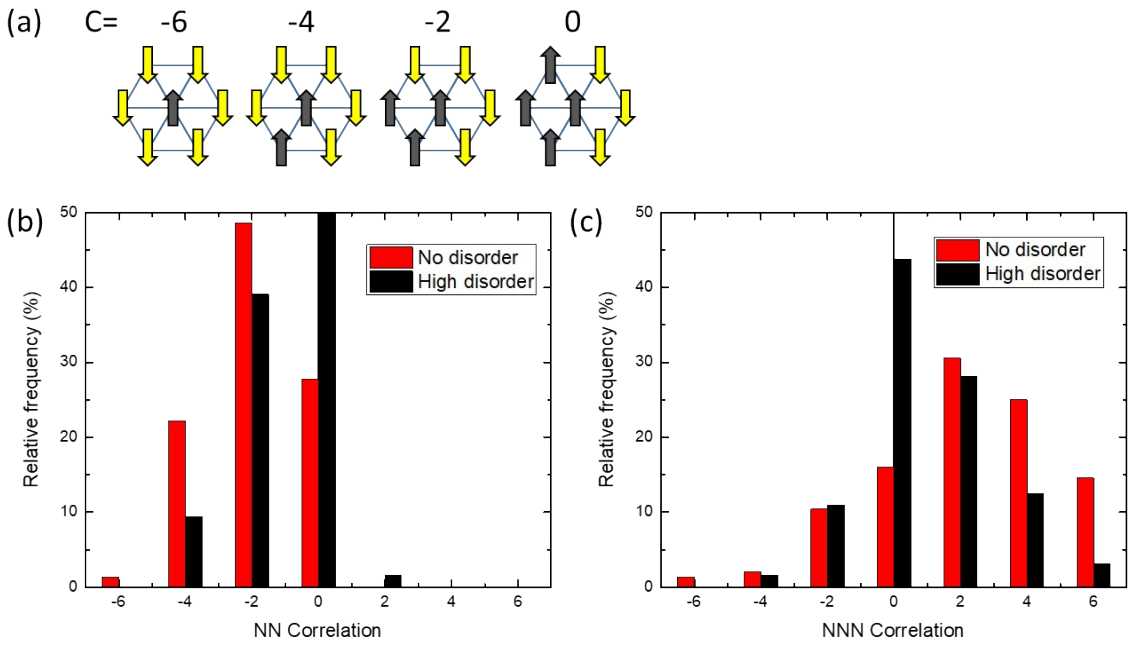

Fig. S13. Correlation coefficients in the depolarized ground state. (a) Graphical representation of the possible values of the correlation coefficient. (b,c) Histogram of the nearest neighbor (NN) and next nearest neighbor (NNN) correlation coefficients for the ground state in Fig. 7. Both the no disorder case (no subcolumns) and the high disorder (mean subcolumn length $N = 7$) are shown.

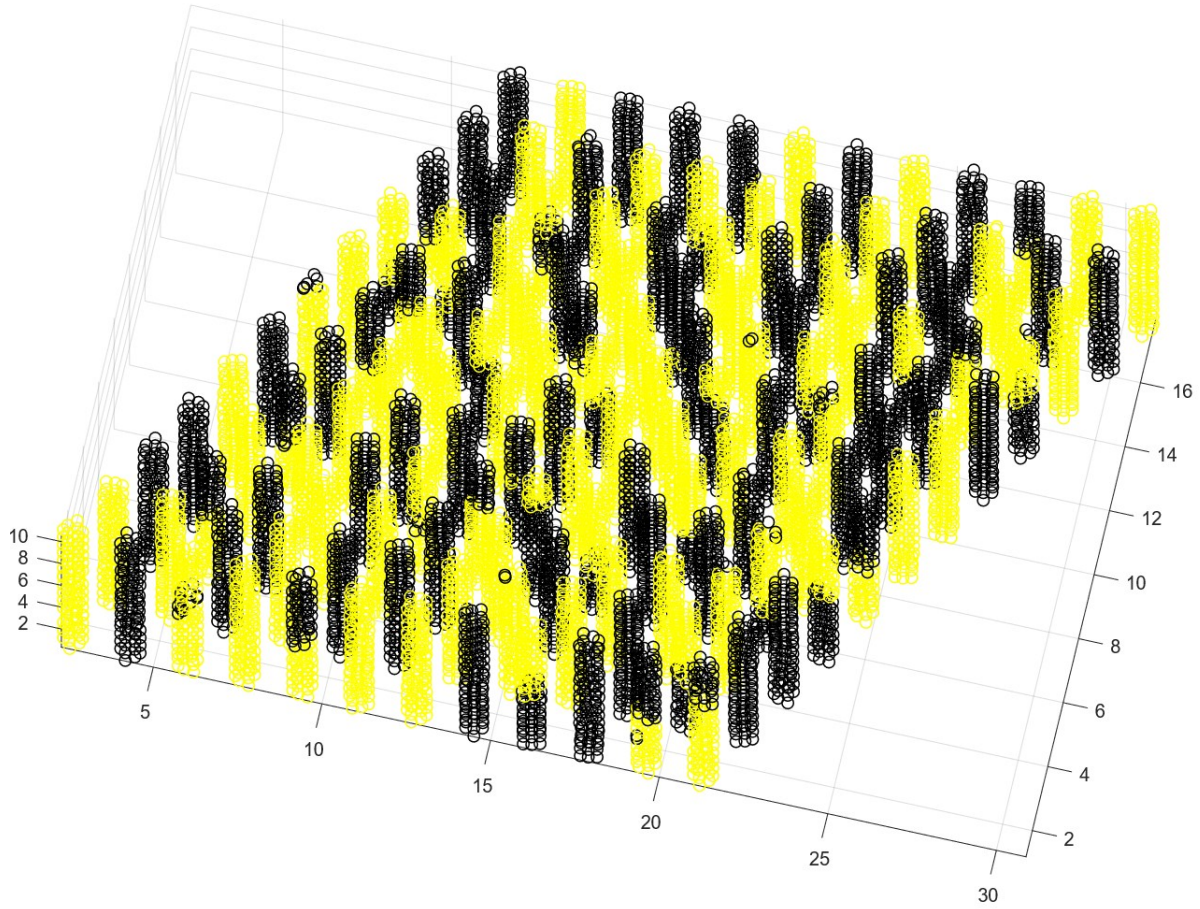

Fig. S14. Domain structure obtained after full depolarization in a system with a high disorder. A tilted top view is chosen to show the partially polarized columns.

References

1 C. J. Fennell and J. D. Gezelter, *J. Chem. Phys.*, 2006, **124**, 234104.

2 A. V. Gorbunov, T. Putzeys, I. Urbanavičiūtė, R. A. J. Janssen, M. Wübbenhorst, R. P. Sijbesma and M. Kemerink, *Phys. Chem. Chem. Phys.*, 2016, **18**, 23663–23672.

3 K. K. Bejagam, G. Fiorin, M. L. L. Klein and S. Balasubramanian, *J. Phys. Chem. B*, 2014, **118**, 5218–5228.

4 K. K. Bejagam, C. Kulkarni, S. J. George and S. Balasubramanian, *Chem. Commun.*, 2015, **51**, 16049–16052.

5 R. Q. Albuquerque, A. Timme, R. Kress, J. Senker and H. W. Schmidt, *Chem. - A Eur. J.*, 2013, **19**, 1647–1657.

6 Gaussian 09, Revision D.01, M. J. Frisch et al., Gaussian, Inc., Wallingford CT, 2013.

7 E. Vanquelef, S. Simon, G. Marquant, E. Garcia, G. Klimerak, J. C. Delepine, P. Cieplak and F.-Y. Dupradeau, *Nucleic Acids Res.*, 2011, **39**, W511–W517.

8 Pigache, A., Cieplak, P. and Dupradeau, F.-Y. *227th ACS National Meeting*, 2004, Anaheim, CA, USA, March 28 - April 1.

9 F.-Y. Dupradeau, A. Pigache, T. Zaffran, C. Savineau, R. Lelong, N. Grivel, D. Lelong, W. Rosanski and P. Cieplak, *Phys. Chem. Chem. Phys.*, 2010, **12**, 7821.

10 Wang, J., Wolf, R. M., Caldwell, J. W., Kollman, P. A. and Case, D. A., *J. Comput. Chem.,* 2004*,* **25**, 1157–1174.

11 D.A. Case *et al.,* 2014, AMBER 2014, University of California, San Francisco.

12 D.A. Case *et al.,* 2016, AMBER 2016, University of California, San Francisco.